*J. Fluid Mech.* (2013), *vol.* 728, *pp.* 396–416. © Cambridge University Press 2013 
doi:10.1017/jfm.2013.214

# Identification of Lagrangian coherent structures in a turbulent boundary layer

**Z. D. Wilson[1], M. Tutkun[2,3] and R. B. Cal[1,†]**

[1]Department of Mechanical and Materials Engineering, Portland State University, Portland, OR 97201, USA

[2]Department of Process and Fluid Flow Technology, Institute for Energy Technology, 2027 Kjeller, Norway

[3]Université Lille Nord de France, École Centrale de Lille, 59655 Villeneuve d'Ascq, France

(Received 18 April 2012; revised 4 December 2012; accepted 22 April 2013; first published online 11 July 2013)

Lagrangian coherent structures (LCS) of a turbulent boundary layer at $Re_\theta$ of 9800 are identified in a plane parallel to the wall at $y^+ = 50$. Three-component high-speed stereo particle image velocimetry measurements on a two-dimensional rectangular plane are used for the analysis. The velocity field is extended in the streamwise direction, using Taylor's frozen field hypothesis. A computational approach utilizing the variational theory of hyperbolic Lagrangian coherent structures is applied to the domain and trajectories are computed using the extended field. The method identified both attracting and repelling Lagrangian coherent structures. There are no apparent differences in distribution of size, orientation and location of attracting and repelling structures. Hyperbolic behaviour appeared in the fluid at and around points of intersection between the attracting and repelling Lagrangian coherent structures. The network of curves identifying distinct regions of coherent flow patterns is displayed in observed relationship between the arrangement of Lagrangian coherent structures and various Eulerian fields.

**Key words:** turbulent flows, turbulent boundary layers

## 1. Introduction

This paper presents the Lagrangian coherent structures (LCS) of a flat-plate turbulent boundary layer at a reasonably high Reynolds number ($Re_\theta = 9800$). Lagrangian coherent structures, as described in Haller (2011) from a physical perspective, are the core material lines and surfaces around which coherent trajectory patterns occur. These structures are based on computing particle trajectories, which lead to a frame-independent, hence objective, description of vortical structures in the flow, cf. Haller (2001, 2005).

One characteristic of turbulent flows is the intense vortical activity, which increases substantially at high Reynolds numbers. As the Reynolds number increases, so do the length of the energy cascade and the ratio of integral scale to dissipative scale. Vortex stretching is the key process in feeding the turbulence cascade with energy, which is extracted from the mean flow by the large scales of motion, cf. Tennekes

† Email address for correspondence: cal@me.pdx.edu

https://doi.org/10.1017/jfm.2013.214 Published online by Cambridge University Press

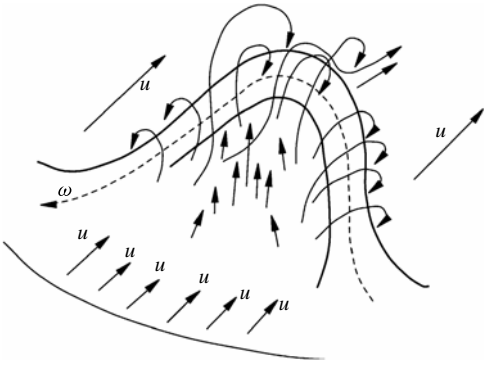



FIGURE 1. Sketch of horseshoe eddy conceptualized by Theodorsen (1952).

& Lumley (1972). Therefore, vortical structures, often called coherent structures, have received much attention in order to understand the underlying dynamics of transfer of the energy from large scales to the smaller ones.

As detailed in a review paper by Adrian (2007), a vast amount of research has been dedicated to visualization, computation and quantification of the coherent structures in wall-bounded flows. Theodorsen (1952), for example, was perhaps the first to propose the horseshoe (or hairpin) vortex as a vortex tube shaped like a horseshoe as seen in figure 1. Even though it was easy to show the vorticity mathematically and describe the vortical structures conceptually, most of the questions stayed open until the advancements in high-resolution direct numerical simulation (DNS) and particle image velocimetry (PIV). These techniques have given researchers access to computing quantities like rate of strain and rate of rotation and to applying quantitative criteria developed to detect coherent structures using all three components of turbulent velocity fluctuations in a highly resolved domain.

Many of the identification strategies involve invariants of the velocity gradient tensor computed from a given instantaneous velocity field, $\boldsymbol{U}$. Methods of this kind include: the $Q$-criterion which requires the second invariant of $\boldsymbol{\nabla U}$ to be greater than a certain threshold (Hunt, Wray & Moin 1988); the $\delta$-criterion which uses the discriminant of the characteristic polynomial of $\boldsymbol{\nabla U}$ to locate regions where $\boldsymbol{\nabla U}$ has complex eigenvalues (Chong, Perry & Cantwell 1990); the swirling strength which is the square of the imaginary part of the complex eigenvalues ($\lambda_{cr} \pm \lambda_{ci}\mathrm{i}$) of $\boldsymbol{\nabla U}$ (Zhou *et al.* 1999); and many others (e.g. Jeong & Hussein 1995; Chakraborty, Balachandar & Adrian 2005). These strategies are considered to be Eulerian because the criterion computed at a location depends on the data (the velocity field in our case) at that location. Many of these strategies to identify vortical structures are frame dependent, cf. Haller (2005).

As an objective tool, Lagrangian coherent structures are studied in various flows in order to extract the frame-independent coherent structures. The past decade has therefore seen a diverse collection of applications involving LCS. They vary from investigations of bio-influenced flows to geophysical flows (Peng & Dabiri 2008; Lukens, Yang & Fauci 2010; Tang, Chan & Haller 2010). In addition, LCS analysis has also been applied in wall-bounded flows: Green, Rowley & Haller (2007) compute direct Lyapunov exponents (DLE, also referred to in LCS literature as finite-time Lyapunov exponents (FTLE)) to capture LCS in a DNS of a turbulent channel flow performed at $Re_\tau$ of 180. Plots of FTLE were compared to swirling strength and the $Q$-criterion for effectiveness of detecting hairpin vortices in a DNS of turbulent channel

https://doi.org/10.1017/jfm.2013.214 Published online by Cambridge University Press

flow. They showed that while FTLE provides more detailed structures in comparison to Eulerian methods, it is also a quantitative way of obtaining structure development. Chong, JinJun & Cao (2009) identified LCS of a low-Reynolds-number turbulent boundary layer ($Re_\theta = 481$) by computing FTLE on the wall-normal–streamwise plane. The results showed that the attracting LCS feature like projections of hairpin vortices on the plane. Investigation of the inclination angle of LCS at three different wall-normal positions ($y^+$ of 15, 55 and 115) yields a $t$-distribution with changing mean value of the inclination angle as the wall-normal position increases. They also noted that the inclination angle saturates at about 24° at $y^+$ of 100. The common conclusion of both studies was the robustness of the LCS with independence from any threshold and quantitative details one can extract from the field.

As briefly touched on above, there are a few different methods to extract LCS from a given velocity field. One of the methods, as introduced by Haller (2001), is to identify surfaces (or curves in two-dimensional flows) that locally optimize the FTLE field for the flow. Shadden, Lekien & Marsden (2005) showed that under certain conditions, the structures identified by this analysis have little fluid flux (computed to first-order) across them, indicating that they track approximately with the fluid. Although this method often locates structures that satisfy a physically intuitive notion of LCS, Haller (2011) gives examples for which this is not the case. Furthermore, Haller (2011) showed that the flux estimate for FTLE ridges is incorrect thus yielding an order-of-magnitude error in the flux computed by the formula of Shadden *et al.* (2005). Employing this formula, Norgard & Bremer (2012) have shown that all LCS would have to be straight lines. A counterargument to the validity of the formula (i.e. ideas expressed by Norgard & Bremer 2012) has been provided in Peikert, Günther & Weinkauf (2013).

Farazmand & Haller (2012*a*) recently introduced a methodology to eliminate false structures captured by the FTLE method using the theory of variational Lagrangian coherent structures, cf. Haller (2011). We therefore use the computational algorithm as proposed by Farazmand & Haller (2012*a*) in order to seek LCS in a plane parallel to the wall and analyse the trajectory patterns in a flat-plate turbulent boundary layer at high Reynolds number.

## 2. Theoretical background

### 2.1. *Lagrangian coherent structures*

Lagrangian coherent structures are material lines and surfaces that delineate coherent trajectory patterns in a flow field. In this section, the theoretical framework for LCS identification in two-dimensional flows is outlined. More detailed descriptions can be found in Haller (2001, 2011) and Shadden *et al.* (2005).

Consider the following dynamical system:

$$\dot{\boldsymbol{x}} = \boldsymbol{U}(\boldsymbol{x}, t), \tag{2.1}$$

where $\boldsymbol{U}(\boldsymbol{x}, t)$ is a smooth vector field defined on an open domain, $D \subset \mathbb{R}^2$, for a finite interval of time, $[a, b]$. For this study, the domain is a horizontal plane in an experimental (wind tunnel) setting and is therefore bounded. For each $\boldsymbol{x}_0 \in D$ and $t_0 \in [a, b]$, there exists a unique trajectory $\boldsymbol{x}(t, t_0, \boldsymbol{x}_0)$, defined for all $t \in [a, b]$, satisfying the initial condition $\boldsymbol{x}(t_0, t_0, \boldsymbol{x}_0) = \boldsymbol{x}_0$. Thus for each pair of times $t_0, t \in [a, b]$, a one-to-one transformation called the *flow map* is defined by

$$\boldsymbol{F}_{t_0}^{t} : D \longrightarrow D \quad \text{and} \quad \boldsymbol{F}_{t_0}^{t}(\boldsymbol{x}_0) = \boldsymbol{x}(t, t_0, \boldsymbol{x}_0). \tag{2.2}$$

https://doi.org/10.1017/jfm.2013.214 Published online by Cambridge University Press

In the context of this study, where $\boldsymbol{U}(\boldsymbol{x}, t)$ is a fluid velocity field, $\boldsymbol{F}_{t_0}^{t}$ can be thought of as a map that describes the evolution of fluid material in the flow. That is, if $M(t_0) \subset D$ is a region occupied by a mass of fluid at time $t_0$, then

$$\boldsymbol{F}_{t_0}^{t}(M(t_0)) = M(t) \tag{2.3}$$

is the region that the mass occupies at time $t$. It is the deformation characteristics of the flow map that are at the heart of LCS identification schemes.

Next, let $\nabla \boldsymbol{F}_{t_0}^{t}(\boldsymbol{x}_0)$ denote the derivative of the flow map at a point $\boldsymbol{x}_0 \in D$. This tensor is non-singular, and in the case that $\boldsymbol{U}$ is incompressible, its determinant is unity (Arnold 1973). The *Cauchy–Green strain tensor* is defined as the positive-definite product of $\nabla \boldsymbol{F}_{t_0}^{t}(\boldsymbol{x}_0)$ and its transpose:

$$\boldsymbol{C}_{t_0}^{t}(\boldsymbol{x}_0) := \nabla \boldsymbol{F}_{t_0}^{t}(\boldsymbol{x}_0)^{\mathrm{T}} \nabla \boldsymbol{F}_{t_0}^{t}(\boldsymbol{x}_0). \tag{2.4}$$

The eigenvalues, $\lambda_1(\boldsymbol{x}_0, t_0, t)$ and $\lambda_2(\boldsymbol{x}_0, t_0, t)$, and eigenvectors, $\boldsymbol{\xi}_1(\boldsymbol{x}_0, t_0, t)$ and $\boldsymbol{\xi}_2(\boldsymbol{x}_0, t_0, t)$, of $\boldsymbol{C}_{t_0}^{t}(\boldsymbol{x}_0)$ can be used to describe flow deformation behaviour up to first-order. Specifically, in linearized flow, a fluid disk centred at $\boldsymbol{x}_0$ at time $t_0$ deforms to be an ellipse centred at $\boldsymbol{F}_{t_0}^{t}(\boldsymbol{x}_0)$ at time $t$, the major and minor axes of which are along $\nabla \boldsymbol{F}_{t_0}^{t}(\boldsymbol{x}_0)\boldsymbol{\xi}_2(\boldsymbol{x}_0, t_0, t)$ and $\nabla \boldsymbol{F}_{t_0}^{t}(\boldsymbol{x}_0)\boldsymbol{\xi}_1(\boldsymbol{x}_0, t_0, t)$, respectively. Furthermore, the disk stretches by a maximum factor of $\sqrt{\lambda_2}$ and a minimum factor of $\sqrt{\lambda_1}$. Since $\boldsymbol{C}_{t_0}^{t}(\boldsymbol{x}_0)$ is positive definite, its eigenvalues satisfy

$$0 < \lambda_1(\boldsymbol{x}_0, t_0, t) \leqslant \lambda_2(\boldsymbol{x}_0, t_0, t), \tag{2.5}$$

and by symmetry of $\boldsymbol{C}_{t_0}^{t}(\boldsymbol{x}_0)$, the eigenvectors can be chosen to form an orthonormal basis. It is also worth noting that in this two-dimensional system, the finite-time Lyapunov exponent is defined as

$$\mathrm{FTLE}(\boldsymbol{x}_0, t_0, t) := \frac{1}{|t - t_0|} \ln\left(\sqrt{\lambda_2(\boldsymbol{x}_0, t_0, t)}\right). \tag{2.6}$$

Of particular interest are material lines, $M$, that either attract or repel nearby fluid over an interval of time, $[t_0, t]$. Repulsion from $M$ over the interval $[t_0, t]$ is evaluated in terms of the *normal repulsion rate* defined at each point $\boldsymbol{x}_0 \in M(t_0)$ by

$$\rho_{t_0}^{t}(\boldsymbol{x}_0, \boldsymbol{n}_0) = \langle \boldsymbol{n}_t, \nabla \boldsymbol{F}_{t_0}^{t}(\boldsymbol{x}_0)\boldsymbol{n}_0 \rangle, \tag{2.7}$$

where $\boldsymbol{n}_0$ is a unit normal to $M(t_0)$ at $\boldsymbol{x}_0$, $\boldsymbol{n}_t$ is a unit normal to $M(t)$ at $\nabla \boldsymbol{F}_{t_0}^{t}(\boldsymbol{x}_0)$, and $\langle \cdot, \cdot \rangle$ is the standard inner product. Mathematically, $\rho_{t_0}^{t}(\boldsymbol{x}_0, \boldsymbol{n}_0)\boldsymbol{n}_t$ is the projection of $\nabla \boldsymbol{F}_{t_0}^{t}(\boldsymbol{x}_0)\boldsymbol{n}_0$ onto the space normal to $M(t)$ at $\boldsymbol{x}(t, t_0, \boldsymbol{x}_0)$ (see figure 2). Hence if $\rho_{t_0}^{t}(\boldsymbol{x}_0, \boldsymbol{n}_0) > 1$, this indicates that an infinitesimal normal perturbation to $M(t_0)$ at $\boldsymbol{x}_0$ moves away from $M$ as time goes from $t_0$ to $t$. Also shown in this figure is $\nabla \boldsymbol{F}_{t_0}^{t}(\boldsymbol{x}_0)\boldsymbol{e}_0$ where $\boldsymbol{e}_0$ is a unit tangent to $M(0)$ at $\boldsymbol{x}_0$. The magnitude of $\nabla \boldsymbol{F}_{t_0}^{t}(\boldsymbol{x}_0)\boldsymbol{e}_0$ is a measure of tangential growth in $M$. If for each $\boldsymbol{x}_0$ along $M(t_0)$, the normal repulsion rate is: (i) greater than this tangential growth; and (ii) greater than 1, then $M$ is defined to be a *normally repelling material line* on $[t_0, t]$. This definition presumes that $t_0 < t$. If on the other hand $t < t_0$, and (i) and (ii) hold for flow backwards in time, then $M$ is defined to be a *normally attracting material line* on $[t, t_0]$.

Loosely speaking, a repelling LCS is the most repelling material core out of a bundle of normally repelling material lines. An analogous description can be made of an attracting LCS. Necessary and sufficient criteria for the existence of a repelling

https://doi.org/10.1017/jfm.2013.214 Published online by Cambridge University Press

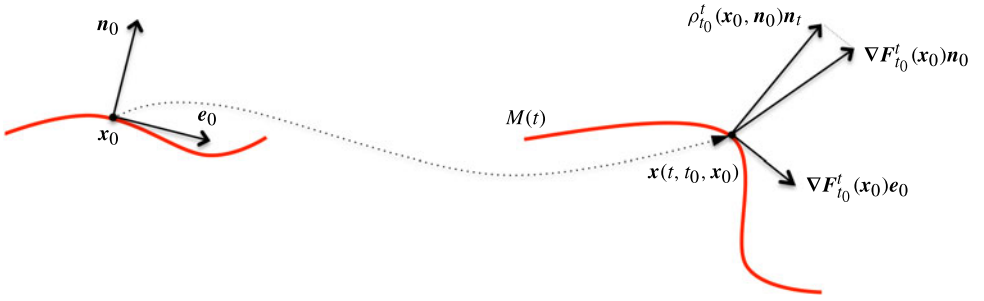



FIGURE 2. (Colour online) Depiction of normal repulsion rate, $\rho^t_{t_0}(\boldsymbol{x}_0, \boldsymbol{n}_0)$.

or attracting LCS over the interval $[t_0, t]$ or $[t, t_0]$ are described in terms of the eigenvalues and eigenvectors of the Cauchy–Green strain tensor as follows (cf. Haller 2011; Farazmand & Haller 2012*b*):

Suppose $M$ is a compact material line and $t_0 < t$. Then $M$ is a repelling LCS over the interval $[t_0, t]$ if and only if for all $\boldsymbol{x}_0 \in M(t_0)$:

(i) $\lambda_1(\boldsymbol{x}_0, t_0, t) \neq \lambda_2(\boldsymbol{x}_0, t_0, t) > 1$;
(ii) $\boldsymbol{\xi}_2(\boldsymbol{x}_0, t_0, t) \perp T_{x_0}M(t_0)$;
(iii) $\langle \nabla\lambda_2(\boldsymbol{x}_0, t_0, t), \boldsymbol{\xi}_2(\boldsymbol{x}_0, t_0, t)\rangle = 0$; and
(iv) $\langle \boldsymbol{\xi}_2, \nabla^2\lambda_2\boldsymbol{\xi}_2\rangle < 0$;

where $T_{x_0}M(t_0)$ is the tangent space to $M(t_0)$ at $\boldsymbol{x}_0$. Similarly, if $t < t_0$, then $M$ is an attracting LCS if and only if conditions (i) to (iv) hold.

Conditions (i) and (ii) characterize curves along which an infinitesimal material disk strains most in its axis normal to the curve. The third and fourth conditions require that this type of straining is locally optimized along $M(t_0)$ relative to 'nearby' curves.

For the purpose of computing LCS from data, the conditions given above are quite restrictive. In particular, the equality of condition (iii) cannot be met exactly, and requires that numerical thresholds be used. Fortunately, these conditions have been reformulated by Farazmand & Haller (2012*a*) to the following:

(i) $\lambda_1(\boldsymbol{x}_0, t_0, t) \neq \lambda_2(\boldsymbol{x}_0, t_0, t) > 1$;
(ii) $\langle \boldsymbol{\xi}_2, \nabla^2\lambda_2\boldsymbol{\xi}_2\rangle \leqslant 0$;
(iii) $\boldsymbol{\xi}_1(\boldsymbol{x}_0, t_0, t) \parallel T_{x_0}M(t_0)$;
(iv) The average value of $\lambda_2$ is maximal on $M(t_0)$ among all nearby curves $\gamma$ satisfying $\boldsymbol{\xi}_1 \parallel \gamma$.

Note that the restrictive pointwise condition $\langle \nabla\lambda_2(\boldsymbol{x}_0, t_0, t), \boldsymbol{\xi}_2(\boldsymbol{x}_0, t_0, t)\rangle = 0$ has been replaced by the condition (iv) in the list. This is essentially applied to curves satisfying the first three reformulated conditions. Note also that being parallel to $\boldsymbol{\xi}_1$ is equivalent to being perpendicular to $\boldsymbol{\xi}_2$.

These reformulated conditions are the ones used in this study because they lead to a robust and implementable technique for identifying LCS from flow velocity data. This is discussed further in § 3.4.

### 2.2. *Extracting LCS from experimental turbulence data*

Computing accurate trajectories, which is crucial for extracting Lagrangian features, from data requires highly time-resolved measurements. This is difficult to achieve

https://doi.org/10.1017/jfm.2013.214 Published online by Cambridge University Press

experimentally on a three-dimensional volume in a turbulent flow, even though there has been tremendous development in obtaining three components of turbulent velocity fluctuations in a volume using tomographic PIV systems. It is more accessible to make time-resolved measurements on a two-dimensional domain in a turbulent flow using a high-repetition stereo PIV system, which provides three components of velocity fluctuations on a plane. Accurate trajectories from this type of data further requires the flow to be quasi-two-dimensional, meaning that the velocity field is dominated by the in-plane component. This is the case for streamwise planes in a turbulent boundary layer.

Consider the trajectory of a particle originating in a quasi-two-dimensional flow field with an out-of-plane velocity component denoted by $V(\boldsymbol{x}, t)$. For a sufficiently small integration time, $T = |t - t_0|$, the true path that the particle takes can be approximated by the in-plane path it takes when $V$ is neglected. For this approximation to be reasonable, the drift away from the plane should be small relative to a local length scale for the direction normal to the plane. In a turbulent flow, this type of requirement can be satisfied statistically as described below.

Let $\tilde{y}$ denote the displacement from the plane of a trajectory that originates in the plane at $t_0$. It should be noted that $\tilde{y}$ is the variable of interest when modelling diffusion by continuous movements from a line source (Pope 2011). The mean and variance of $\tilde{y}$ can be expressed in terms of the statistics for $V$ by considering the following integral equation:

$$\tilde{y}(t, t_0, \boldsymbol{x}_0) = \int_{t_0}^{t} V(\tilde{\boldsymbol{x}}(s, t_0, \boldsymbol{x}_0), s)\, \mathrm{d}s, \tag{2.8}$$

where $\tilde{\boldsymbol{x}}(s, t_0, \boldsymbol{x}_0)$ is the true path the particle takes. It follows that the mean and variance are given respectively by:

$$\langle \tilde{y}(t, t_0, \boldsymbol{x}_0) \rangle = \int_{t_0}^{t} \langle V(\tilde{\boldsymbol{x}}(s, t_0, \boldsymbol{x}_0), s) \rangle\, \mathrm{d}s \tag{2.9}$$

and

$$\langle (\tilde{y}(t, t_0, \boldsymbol{x}_0) - \langle \tilde{y}(t, t_0, \boldsymbol{x}_0) \rangle)^2 \rangle = \int_{t_0}^{t} \int_{t_0}^{t} \langle v(\tilde{\boldsymbol{x}}(s, t_0, \boldsymbol{x}_0), s) v(\tilde{\boldsymbol{x}}(s', t_0, \boldsymbol{x}_0), s') \rangle\, \mathrm{d}s\, \mathrm{d}s' \tag{2.10}$$

where $v = V - \langle V \rangle$. Therefore, an appropriate integration time can be determined from the statistical behaviour of the out-of-plane velocity component. In terms of order of magnitude: $\langle \tilde{y} \rangle \sim \langle V \rangle T$; and assuming that the Lagrangian autocorrelation for $V$ remains significant on the interval $[t_0, t]$, the drift variance can be estimated by $\langle (\tilde{y} - \langle \tilde{y} \rangle)^2 \rangle \sim \langle v^2 \rangle T^2$ (Pope 2011).

## 3. Description of data and methods

### 3.1. *Data*

The data used in this study come from time-resolved, high-repetition, stereo particle image velocimetry, taken on a plane parallel to the wall in a flat-plate turbulent-boundary-layer wind tunnel experiment. The experiments took place in the Laboratoire de Mécanique de Lille (LML) in Lille, France. The wind tunnel in this facility can provide a high-Reynolds-number boundary layer with an approximate thickness of 0.3 m. The test section is 20.6 m long, with a 2 m wide by 1 m high cross-section. The length is composed of a 15.6 m boundary layer development section followed by

https://doi.org/10.1017/jfm.2013.214 Published online by Cambridge University Press

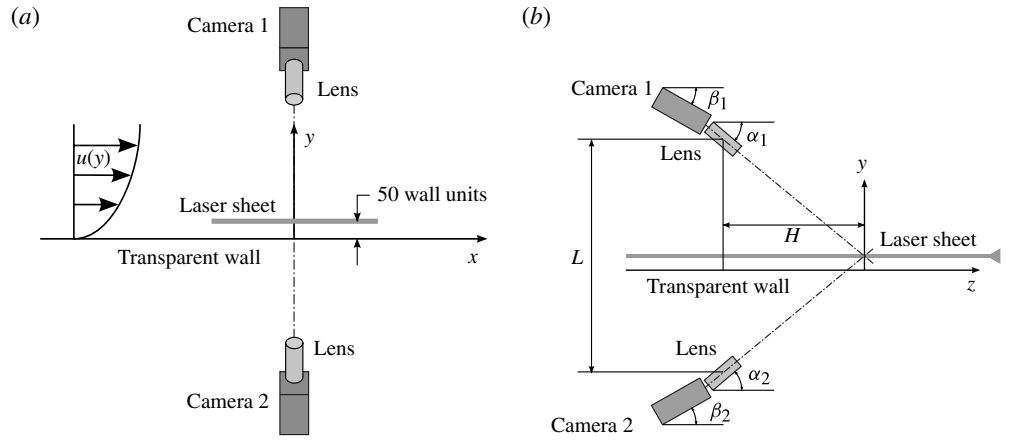



FIGURE 3. Experimental setup: (*a*) view from the positive-$z$ side; (*b*) view from upstream.

a 5 m transparent test section. The free-stream velocity can be continuously adjusted from 0 to 10 m s$^{-1}$. A detailed description of the wind tunnel and flow characteristics is given in Carlier & Stanislas (2005).

Figure 3 illustrates the experimental setup, which is described in full detail in Foucaut *et al.* (2007). The $x$- and $z$-axes are along the streamwise and spanwise directions respectively. The two cameras are VisionResearch Phantom V9.0, located opposite to the laser in order to be in symmetrical forward-scattering conditions. The parameters are $H = 1.15$ m and $L = 2.06$ m. A 200 mm focal lens is used on each camera with $f\# = 4$. The cameras are set in Scheimpflug conditions. The light sheet is generated by two ExcelTechnology Darwin pulsed YLF lasers. The thickness of the laser sheet is $\sim$1 mm or roughly 10 viscous lengths. The flow is seeded with poly-ethylene glycol, and the particle size is of the order of 1 μm.

Measurements are taken in a flow with a free-stream velocity ($U_\infty$) of 5 m s$^{-1}$, which corresponds to a Reynolds number based on momentum thickness ($Re_\theta$) of 9800 at a streamwise location 18.9 m downstream of the inlet of the test section. At the measurement location the boundary layer thickness ($\delta$) is approximately 0.3 m. The measurement region is a plane, 5.9 cm in the streamwise ($x$) direction by 4.8 cm in the spanwise ($z$) direction, parallel to the wall at $y = 4.5$ mm, which corresponds to 50 wall units, where viscous length (one wall unit) is defined as $\delta_\nu = \nu/u_\tau$. Figure 4 shows a plot of one frame of velocity data. The sampling frequency of the measurement is 1500 Hz, yielding a time resolution d$t$ of 0.67 ms. The spatial resolution is d$x$ = d$z$ = 0.5 mm. A total of 1200 packets of 40 time-resolved fields are recorded in order to compute the statistics.

Variations in particle trajectories are dictated by the dynamics of the fluctuating velocity field, $\boldsymbol{u} = \boldsymbol{U} - \langle \boldsymbol{U} \rangle$. Therefore, the primary velocity scale becomes the friction velocity, $u_\tau = 0.174$ m s$^{-1}$, which is of the same order of magnitude as the fluctuations in this study. The corresponding viscous length, $\delta_\nu = 0.09$ mm. The location of the measurement plane in the wall-normal direction ($y$) is such that $\delta_\nu \ll y \ll \delta$ by factors of 50 ($y = 50\delta_\nu$) and 67 ($y \approx \delta/67$) respectively. Note that $y$ itself is the primary length scale relevant to the dynamics herein (Tennekes & Lumley 1972). Therefore, an integration time ($T$) taken as $y/u_\tau$ and is determined to be sufficient

https://doi.org/10.1017/jfm.2013.214 Published online by Cambridge University Press

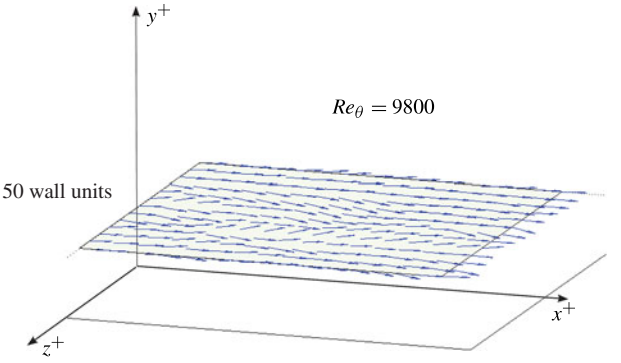



FIGURE 4. (Colour online) Plot of a time frame of velocity data.

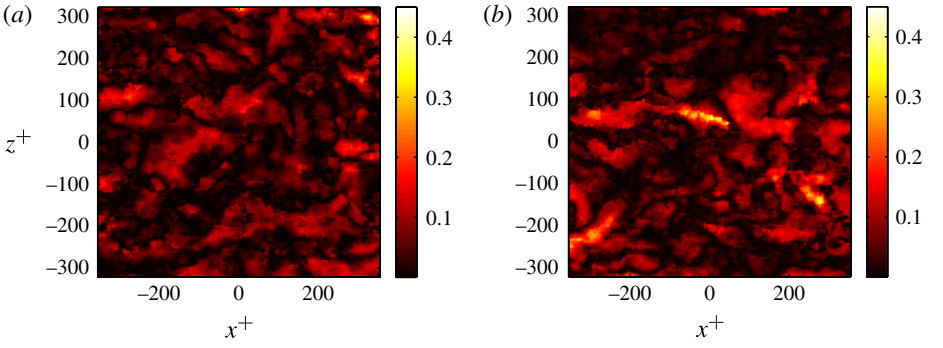



FIGURE 5. (Colour online) Instantaneous ratio $\sqrt{V^2}/\sqrt{U^2 + W^2}$ at two different times: (*a*) the best two-dimensionality; (*b*) the least two-dimensionality.

to capture significant Lagrangian features. Note that the resulting integration time $T = 25.8$ ms $\approx 39\,\mathrm{d}t$, where 40 time steps are used in the analysis.

Another aspect of setting up the experiment using a wind tunnel with a long test section and operating the tunnel at low velocity is that the evolution of flow structures should be slow in comparison to the evolution of the trajectories in order for the structures to qualify as LCS. Additionally, a long test section with low operating speeds ensures that the turbulence scales grow slowly as the boundary layer develops over the wall and consequentially results in a slow evolution, or large-scale eddy turnover time, of the structures. On the other hand, the characteristic time scale of the trajectories is of the order of the integration time, which is found to be at least one order of magnitude smaller than the time scale governing the evolution of flow structures.

### 3.2. *Assessment of the two-dimensional flow assumption*

In this analysis, the flow is treated as quasi-two-dimensional even though the turbulent boundary layer structures are inherently three-dimensional. To justify this approach, the ratio of the out-of-plane velocity magnitude to the in-plane velocity magnitude, $\sqrt{V^2}/\sqrt{U^2 + W^2}$, is computed for each time frame. Figure 5 shows plots of this value respectively demonstrating the most and least two-dimensionality over the time frames

https://doi.org/10.1017/jfm.2013.214 Published online by Cambridge University Press

of data. The average ratio is 0.05. Note that as a rare event larger ratios are also observed, but with no significant effect on the average. This average, being much less than 1, indicates that the velocity is dominated by the in-plane component.

The above computation shows the instantaneous vector fields to be quasi-two-dimensional. In addition to this, as discussed in § 2.2, a sufficiently small integration time must be chosen so that real trajectories do not have significant vertical displacement. In this study, with the chosen integration time, the expected particle displacement from the plane is approximated as $\langle V \rangle T \approx 4\delta_\nu$. This is significantly less than the local length scale, $y = 50\delta_\nu$, and of the order of the spatial resolution.

As also detailed in Garth *et al.* (2007), the negligible out-of-plane velocity component ensures that the largest separation of neighbouring trajectories under the action of unstable hyperbolic manifold lies in the same plane. This separation indeed determines what value the finite-time Lyapunov exponent attains. This essentially leads to no significant difference between computing the structures in a three-dimensional volume or a two-dimensional plane provided that the flow is dominated by the in-plane component.

Another assessment of two-dimensionality can be made, after trajectories are computed, by evaluating the Lagrangian divergence, defined by

$$L_{t_0}^{t}(\boldsymbol{x}_0) = \int_{t_0}^{t} \boldsymbol{\nabla} \cdot \boldsymbol{U}(\boldsymbol{x}(s, t_0, \boldsymbol{x}_0), s)\, \mathrm{d}s. \tag{3.1}$$

As mentioned in Mathur *et al.* (2007), the exponential of the Lagrangian divergence, $\exp(L_{t_0}^{t}(\boldsymbol{x}_0))$, is the factor by which infinitesimal areas are magnified. For a truly two-dimensional incompressible flow, the value of $\exp(L_{t_0}^{t}(\boldsymbol{x}_0))$ should be 1 at each point. For the data in this study, the mean of this value is close to 1.0 over the domain. The large values occur only in small isolated sections of the domain in particular close the the edges, and therefore the mean value over the entire domain is 1.2. In other words, in-plane stretching along one direction is balanced by convergence along another in-plane direction as opposed to an out-of-plane direction. Since the LCS method employed here for detecting structures analyses in-plane stretching, the Lagrangian divergence is an appropriate check for two-dimensionality. Further description, justification and application of extraction of two-dimensional LCS from the three-dimensional data can be found in Tallapragada, Ross & Schmale (2011) and Tang, Chan & Haller (2011). Furthermore, the transport of particles, which essentially forms the backbone of the analysis detailed, is governed by the large-scale structures in the flow. These large scales are also responsible for large-scale mixing, which also closely relates to the present analysis. Owing to the nature of these structures, most of their characteristics are indeed reflected on a two-dimensional plane that cuts through the structures. Consequently, this ensures that the obtained solution reflects the behaviour of structures on a plane.

### 3.3. *Data extension*

In order to compute trajectories on a limited domain of data, a combination of techniques to extend the velocity field beyond the measurement domain is used. In particular, Taylor's hypothesis (originally described in Taylor 1938) is applied to extend the domain in the streamwise direction, which is the dominant and convective flow direction. This allows for the computation of most of the trajectories whose initial points are in the data domain.

https://doi.org/10.1017/jfm.2013.214 Published online by Cambridge University Press

There are, however, some trajectories that exit this streamwise extended domain, particularly those initiating at the spanwise boundaries of the data domain. It is important that these trajectories continue in a manner that does not yield falsely high partial derivatives of the flow map, because such derivatives would introduce spurious eigenvalue maxima. This is precisely what is accomplished by the velocity field extension method of Tang *et al.* (2010). This method computes, at each time, the $(C^0)$-closest linear divergence-free approximation to a velocity field on a rectangular domain. At the boundary of the domain, there is a smooth transition to this linear field, which is the velocity field to be used for trajectories that exit the rectangular domain.

Taylor's hypothesis, also described as the 'frozen turbulence' assumption, asserts that if convection velocity, $U_c$, is much larger than turbulent fluctuations, then variation in time and variation in space are related by the following (Hinze 1959):

$$\frac{\partial}{\partial t} = -U_c \frac{\partial}{\partial x} \tag{3.2}$$

where $x$ is the direction of the convection velocity. This relation implies that $\boldsymbol{U}(\boldsymbol{x}, t) = \boldsymbol{U}(\boldsymbol{x} + (U_c\tau)\boldsymbol{e}_x, t + \tau)$, where $\boldsymbol{e}_x$ is the unit vector in the $x$-direction. Therefore, in a flow for which Taylor's hypothesis holds, velocity data can be extended downstream at 'later' times ($\tau > 0$) and upstream at 'earlier' times ($\tau < 0$).

There has been extensive research on the validity of Taylor's hypothesis in the turbulent boundary layer and methods for determining the convection velocity (Dennis & Nickels 2008; Álamo & Jiménez 2009). The validity of the assumption has been observed in turbulent flows, including wall-bounded flows, extending to 6–7 boundary layer thicknesses. As this distance is exceeded, the turbulence structures are affected by the application. Therefore the extended field in the streamwise direction in this study is well below the upper limit. With velocity measurements taken over space and time at a fixed $y$, the degree to which $U(x, z, t) = U(x + U_c\tau, z, t + \tau)$ and $W(x, z, t) = W(x + U_c\tau, z, t + \tau)$ hold true, for the flow in this study, can be checked directly. To do this, the convection velocity, $U_c$, is taken to be the mean streamwise velocity over space and time, and the following are checked: (i) at a given streamwise location and time, $(x, t)$, the velocity profiles $U$ and $W$ along $z$ are highly correlated with the respective profiles downstream and later in time at $(x + U_c\,\mathrm{d}t, t + \mathrm{d}t)$, where $\mathrm{d}t$ is the time resolution of the data; and (ii) the *coefficients of determination* for $U$ and $W$ are both close to 1. These values, also known as $R^2$ values, are computed as

$$R_u^2 = 1 - \frac{\displaystyle\sum_{x,z,t} (u(x + U_c\,\mathrm{d}t, z, t + \mathrm{d}t) - u(x, z, t))^2}{\displaystyle\sum_{x,z,t} u(x, z, t)^2}, \tag{3.3}$$

$$R_w^2 = 1 - \frac{\displaystyle\sum_{x,z,t} (w(x + U_c\,\mathrm{d}t, z, t + \mathrm{d}t) - w(x, z, t))^2}{\displaystyle\sum_{x,z,t} w(x, z, t)^2}, \tag{3.4}$$

where the summation is taken over 574 938 space–time datum points, $(x, z, t)$, and the lower-case $u$ and $w$ refer to fluctuations in the streamwise and spanwise directions respectively: $u = U - \langle U \rangle$ and $w = W - \langle W \rangle$.

Condition (i) ensures that the general shapes of the profiles are being advected downstream. This is illustrated in figure 6 for a selected $(x, t)$ pair. In this figure, $z$

https://doi.org/10.1017/jfm.2013.214 Published online by Cambridge University Press

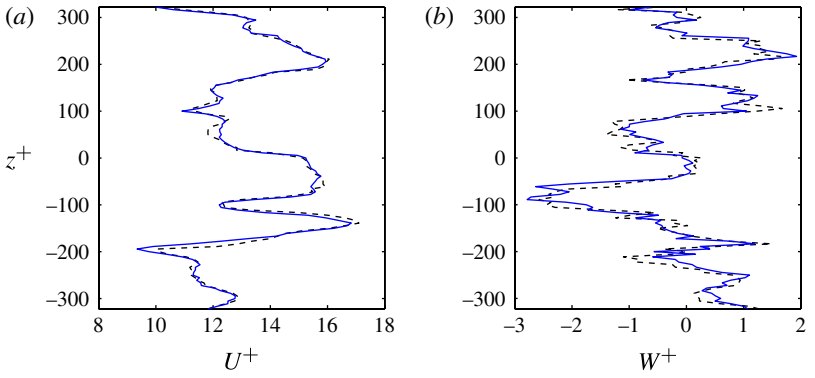



FIGURE 6. (Colour online) $U$ (streamwise) and $W$ (spanwise) velocity profiles together with extended profiles using Taylor's hypothesis: (*a*) $U^+(x + U_c\,\mathrm{d}t, t + \mathrm{d}t)$ (solid line) compared to $U^+(x, t)$ (dashed line); (*b*) $W^+(x + U_c\,\mathrm{d}t, t + \mathrm{d}t)$ (solid line) compared to $W^+(x, t)$ (dashed line).

is normalized by $\delta_v$ and the velocities are normalized by $u_\tau$. Condition (ii) checks, globally, that $\boldsymbol{U}(x + U_c\,\mathrm{d}t, z, t + \mathrm{d}t)$ is well predicted by $\boldsymbol{U}(x, z, t)$. That is, the mean error associated with this prediction is small relative to the variance in velocity. For the data used in this study, $R_u^2 = 0.97$ and $R_w^2 = 0.89$, indicating that the extension provides sufficiently good data in order to enlarge the field.

These two velocity extension techniques are incorporated in the following manner. Velocity fields are computed on a moving rectangular domain, $D(t)$, by using measured data where it is available and using Taylor's hypothesis where data are not available. This field is then extended to an infinite plane by the technique of Tang *et al.* (2010). The rectangle, $D(t)$, is intended to move with the bulk of the flow, hence it moves in the streamwise direction with velocity $U_c$. In the following outlined description, let $\boldsymbol{U}(t)$ be the velocity field defined on $D(t)$, let $\boldsymbol{V}_L(t)$ be the $(C^0)$-closest linear divergence-free approximation to $\boldsymbol{U}(t)$, let $\boldsymbol{V}(t)$ be the extended field that transitions from $\boldsymbol{U}(t)$ on $D(t)$ to $\boldsymbol{V}_L(t)$ outside of $D(t)$, and let $\boldsymbol{U}_{data}(t)$ be the velocity data measured at time $t$, which are on a fixed domain.

(i) At the initial time, $t_0$, $D(t_0)$ is the data domain and $\boldsymbol{U}(t_0) = \boldsymbol{U}_{data}(t_0)$.

(ii) For each time step, $D(t + \mathrm{d}t) = D(t) + (U_c\,\mathrm{d}t, 0)$; in other words, the domain shifts by $U_c\,\mathrm{d}t$ in the streamwise direction. This shift is small enough that for at all but the last few time steps, the moving domain intersects the data domain. On the section of $D(t + \mathrm{d}t)$ that intersects the data domain, $\boldsymbol{U}(t + \mathrm{d}t) = \boldsymbol{U}_{data}(t + \mathrm{d}t)$. On the section of $D(t + \mathrm{d}t)$ that does not intersect the data domain, $\boldsymbol{U}(x + U_c\,\mathrm{d}t, z, t + \mathrm{d}t) = \boldsymbol{U}(x, z, t)$.

(iii) After establishing $\boldsymbol{U}(t)$, on $D(t)$, this field is extended to $\boldsymbol{V}(t)$, which is used to advance each trajectory.

### 3.4. *LCS computation*

The LCS are computed using a sequence of start times on a fixed rectangular domain, $D_0$ (which is slightly smaller and in the interior of the measurement domain). The method for computing LCS in this study follows that described in Farazmand & Haller (2012*a*), which is based on a reformulation of the LCS conditions discussed above in § 2.1. This method is implemented for each start time, $t^+$ (time being non-

https://doi.org/10.1017/jfm.2013.214 Published online by Cambridge University Press

dimensionalized by $\tau = \delta_v/u_\tau$), to the interval $[t^+ - 50, t^+]$ for attracting LCS and the interval $[t^+, t^+ + 50]$ for repelling LCS. The steps are outlined as follows (the start and end times are being suppressed from notation):

(i) compute the fields $\lambda_1, \lambda_2, \boldsymbol{\xi}_1$, and $\boldsymbol{\xi}_2$ on the domain $D_0$;

(ii) identify the subset $D_1 \subset D_0$ on which $\lambda_1 \neq \lambda_2 > 1$ and $\langle \boldsymbol{\xi}_2, \nabla^2\lambda_2\boldsymbol{\xi}_2\rangle \leqslant 0$;

(iii) find curves in $D_1$ that are tangent to the vector field $\boldsymbol{\xi}_1$;

(iv) from this collection of curves, select the ones that exhibit locally the highest average value of $\lambda_2$.

Here the average value of $\lambda_2$ along a curve $\gamma$ with length $l$ is defined as

$$\bar{\lambda}_2(\gamma) = \frac{1}{l}\int_\gamma \lambda_2(\boldsymbol{x})\,\mathrm{d}s. \tag{3.5}$$

Step (iii) is implemented by solving a time delay system whose trajectories are parallel to the field $\boldsymbol{\xi}_1$. A time delay system is needed because the field $\boldsymbol{\xi}_1$ can have singularities at which the direction reverses discontinuously. Therefore, at each integration step, the directions of $\boldsymbol{\xi}_1$ at the current and previous steps are compared to see if such a reverse has taken place. If a reverse of direction is detected, the negative of the field is then followed. This problem and the strategy for its solution are described in detail by Farazmand & Haller (2012*a*). In this study, the initial points of these trajectories are chosen to be the points in $D_1$ that locally maximize $\lambda_2$ along the $\boldsymbol{\xi}_2$-direction. Solving this system then results in several clusters of overlapping curves. The curves that are less than $100\delta_v$ in length are discarded as they often appeared to be the result of computational error rather than turbulent structures.

At this point in the process, the clusters of curves that have been obtained are bundles of normally repelling/attracting material lines. Indeed, because of the way that they are oriented, which is the result of step (iii), the normal repulsion rate is equal to $\sqrt{\lambda_2}$. Therefore, the last step is to select the most repelling/attracting core of each bundle. The bundles are identified as groups of curves that have similar lengths and proximities. This is measured with three parameters: length, centre $x$ location, and centre $z$ location, defined respectively as follows (here $\gamma$ denotes a curve):

$$l(\gamma) = \int_\gamma \mathrm{d}s, \quad \bar{x}(\gamma) = \int_\gamma x\,\mathrm{d}s, \quad \bar{z}(\gamma) = \int_\gamma z\,\mathrm{d}s. \tag{3.6}$$

Although this is a simple metric by which to group curves, it is possible that two very different curves have similar length and $(\bar{x}, \bar{z})$ location. Therefore several time frames are checked manually to determine how similar $(l, \bar{x}, \bar{z})$ must be to not group curves of different bundles.

From each group, the curve that has the highest average value of $\lambda_2$ is selected as an LCS. Some of the selected curves may still appear similar, but often they have portions that are distinct from each other. This results in an apparent overlap that can be observed in the plots of § 4 as curves that appear thicker than others.

## 4. Results and discussion

### 4.1. *Description of computed LCS*

The application of the algorithm described above identifies several coherent structures distributed about the domain. Figure 7 shows an assortment of attracting LCS in blue and repelling LCS in red. They advect with time, demonstrating a temporal coherence.

https://doi.org/10.1017/jfm.2013.214 Published online by Cambridge University Press

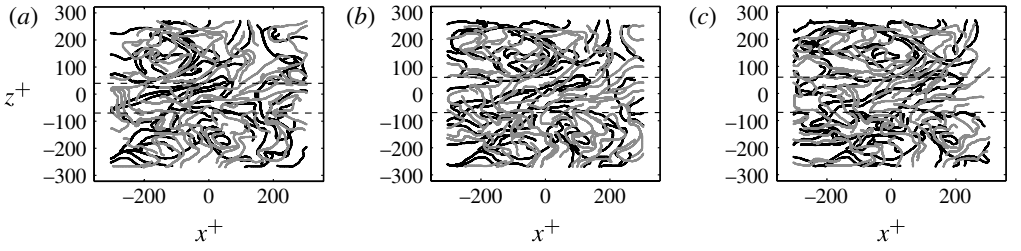



FIGURE 7. Lagrangian coherent structures computed at a sequence of three times: (*a*) $t^+ = 1.29$; (*b*) $t^+ = 6.46$; (*c*) $t^+ = 11.6$.

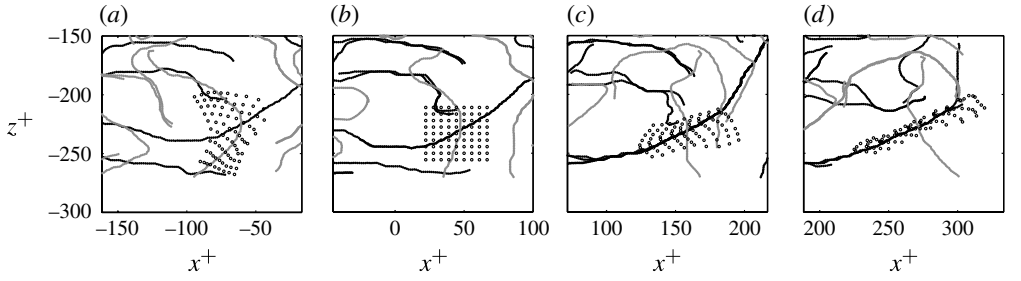



FIGURE 8. Hyperbolic behaviour at an intersection of a repelling and attracting LCS: (*a*) $t^+ = 3.88$; (*b*) $t^+ = 12.92$; (*c*) $t^+ = 21.97$; (*d*) $t^+ = 31.01$.

Some curves traverse the entire domain, while others disappear (and in some cases reappear). As they flow, they also evolve, i.e. making slight changes in length and orientation and in several cases structures breaking up or combining with each other. From a global perspective, the curves form intricate tangles and networks whose patterns can be identified in sequential time frames. This time coherence at various scales is significant as it indicates that LCS computed over the interval $[t_0+\Delta t, t_1+\Delta t]$ approximate the advection of LCS computed over the interval $[t_0, t_1]$ under the flow map $F_{t_0}^{t_0+\Delta t}$ for noticeable durations of time, $\Delta t$, in a turbulent boundary layer.

Lagrangian coherent structures are captured in figure 7 at a sequence of three time steps. The captured LCS structures appear to be organized into two different types of layers across the spanwise direction: at the top and the bottom are layers of round tumbleweed-like networks formed by curves of various orientation and curvature; in the middle is a layer of curves that run predominantly in the streamwise direction. These two types of layers are identifiable in all time frames and are typically $100\delta_\nu$ to $200\delta_\nu$ wide. The arrangement of the layers across the domain changes with time. For instance, at the bottom left of figure 7(*c*), the beginning of a layer of streamwise LCS can be seen.

### 4.2. *Coherent trajectory patterns*

When studying the trajectory patterns near the LCS, seeding a specified domain and investigating behaviour of the flow of seeds relative to the structures is found to be very useful. For that purpose, a 9 by 9 grid of seeds starts at an intersection of a repelling LCS (in black) and an attracting LCS (in gray) with approximately vertical and horizontal orientations respectively (figure 8*b*). As time increases, the seeds move towards and spread out along the attracting LCS. This attraction is best shown in figure 8(*d*). The repelling LCS acts as a boundary, determining whether

https://doi.org/10.1017/jfm.2013.214 Published online by Cambridge University Press

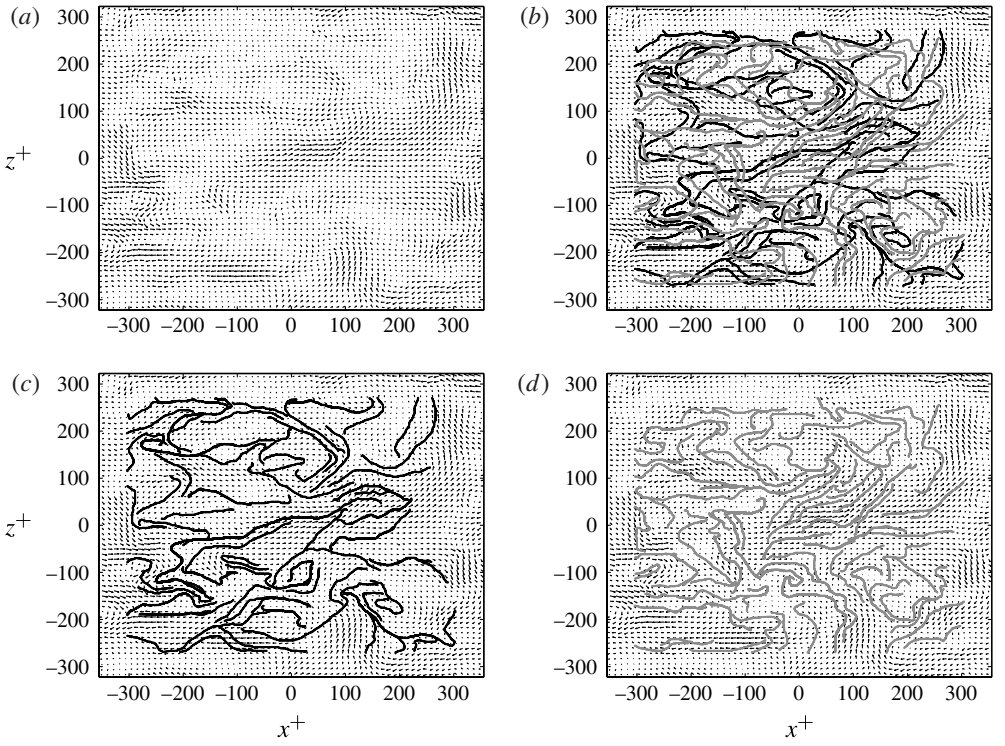



FIGURE 9. Lagrangian coherent structures compared with the fluctuating velocity field at $t^+ = 11.6$: (*a*) fluctuating velocity field; (*b*) LCS over fluctuating velocity field; (*c*) attracting LCS over fluctuating velocity field; (*d*) repelling LCS over fluctuating velocity field.

seeds move left or right along the attracting LCS. The most predictable behaviour is the hyperbolicity that occurs at intersections between repelling and attracting LCS. Figure 8 shows the trajectory pattern near one of these intersections. This hyperbolic behaviour, in which the fluid contracts normal to the attracting LCS and stretches normal to the repelling LCS, was observed at several intersections of attracting and repelling LCS.

### 4.3. *Turbulent structures depicted by LCS*

The Lagrangian structures extracted in this study lie along boundaries between dynamically distinct regions. This can be seen in figure 9 in which the arrangement of the LCS is compared with the fluctuating velocity field all at a fixed time ($t^+ = 11.6$). The LCS tend to approximate separatrices in the fluctuating field, which is separately shown in figure 9(*a*). While many of the LCS lie tangent to the fluctuating field, some are oriented roughly perpendicular to it. Such structures often mark locally objective distinctions between 'fast' and 'slow' moving fluid. As an example, the fluid that is approximately at the centre of the domain at the time depicted in figure 9 demonstrates this type of behaviour. Here, the direction of the flow is parallel to an attracting LCS (figure 9*c*), while nearby repelling LCS run transversely to this direction. Consequently, the fluid is accelerating along the direction of the flow. Following this direction for $\sim 100\delta_v$, it can be seen that the opposite is true: the

https://doi.org/10.1017/jfm.2013.214 Published online by Cambridge University Press

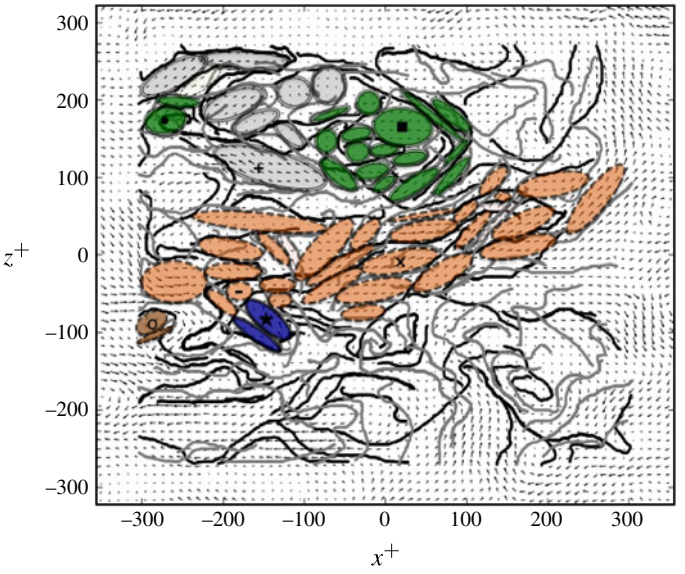



FIGURE 10. (Colour online) Network of LCS reveals multiple scales of structure in the fluctuating velocity field, corresponding to figure 9(*b*).

flow becomes decelerating as it runs parallel to nearby repelling LCS, and transversely to attracting LCS.

In the light of their relationship to the fluid velocity field, the organization of the LCS complies well with the current understanding of the turbulent boundary layer. The longer straighter LCS, which tend to be oriented in the streamwise direction, often correspond to regions of relatively high or low streamwise momentum. Collectively, these types of curves form layers (as noted in § 4.1) that are $100\delta_\nu$ to $200\delta_\nu$ wide in the spanwise direction and sometimes more than $600\delta_\nu$ (or nearly $0.2\delta$, where $\delta$ is the boundary layer thickness) in the streamwise direction. These layers are the largest scale of organization identified in this study.

The LCS identify various ways in which structures of smaller scales combine to form larger-scale structures in the instantaneous velocity fields. Figure 10 demonstrates the organization of these structures in the fluctuating velocity field at $t^+ = 11.6$, which corresponds to the same instant in time as figure 9. The partially transparent ovals are added to aid the discussion. Note that the same plot can can be viewed objectively (without the ovals) in figure 9(*b*).

At the level of the smallest scales ($50\delta_\nu$ to $100\delta_\nu$), the tangles of LCS encompass regions that can be categorized as 'spurts', 'swirls', and 'stagnations'. The relatively large light grey-double line oval at $(x^+, z^+) = (-150, 125)$ highlights a spurt denoted by the symbol $+$. The spurts exhibit heightened turbulent kinetic energy and have approximately parallel fluctuations. A swirl can be seen at $(x^+, z^+) = (-280, -100)$ highlighted by symbol $\bigcirc$. Swirls are characterized by having non-zero swirling strength. Stagnations have near zero fluctuations. An example of this is marked by symbol $-$ and the coordinates are $(x^+, z^+) = (-175, -40)$. In several cases, adjacent spurts appear in hyperbolic areas of the fluctuating field. The pair of solid lined ovals marked by $\star$ (dark blue) at about $(x^+, z^+) = (-140, -100)$ highlights an example of this. Another common grouping is a spurt running roughly tangent to

https://doi.org/10.1017/jfm.2013.214 Published online by Cambridge University Press

a swirl. Such behaviour is marked by a pair of dashed lined marked by ○ ovals at $(x^+, z^+) = (-280, -100)$ and a pair of solid double line ovals marked by ● at $(x^+, z^+) = (-275, 190)$ (green).

These regions organize into groups to form larger structures as well. Examples are: the dashed lined ovals (light orange) between $x^+ = -250$ and 250 and $z^+ = -75$ to 100 marking a collection of mostly elongated spurts in the middle spanwise layer (centred around ×); and between $x^+ = -100$ and 100 and $z^+ = 60$ to 220 a cluster of regions, marked by solid double lined ovals and symbol ■ (green), that depicts a rotational structure $\sim 200\delta_\nu$ in diameter. In this second structure, spurts run clockwise around the structure, while stagnations lie in its core. A similar structure (not marked by ovals) can be observed in the lower right part of the plot.

These mesoscale structures can sometimes be seen as substructures of larger patterns. This is the case for the dark shaded solid double line cluster, centred at (0, 140), noted above, which appears to be part of a larger structure marked by all double lined ovals and include symbols ●, + and ■. These larger structures identify spatial coherences that are often difficult (if not impossible) to detect from a single frame of velocity data. Recall that a single frame of LCS incorporates several frames of velocity data.

It is evident from the plots of the LCS over the fluctuating velocity field that there are relationships between the Lagrangian structures identified in this study and Eulerian structures that can be identified in fields computed from instantaneous data. To further explore this, the attracting and repelling LCS are compared to plots of the streamwise velocity (figure 11*a,b*) and the quantity $(u^2 + v^2 + w^2)/2u_\tau^2$) (figure 11*c,d*), which represents the instantaneous contribution to turbulent kinetic energy. These figures show a general relationship between the arrangement of LCS and the contour topology of the two fields.

Compared to these two Eulerian fields, the attracting and repelling LCS appear to have similar spatial arrangements. Most of the Eulerian structures are identified by a combination of repelling and attracting LCS. Both high-momentum zones and low-momentum zones tend to be traced out by LCS; however the interior of the high-momentum zones possesses more intricate networks of substructures marked by LCS within the zones.

Figures 12 and 13 compare the LCS to contours of swirl strength (normalized by $1/\tau^2$) and the fluctuating velocity field. The sign of the swirl strength indicates direction of rotation with counterclockwise being the positive direction. (Note that the background value, ≈0, has been removed for clarity.) Figure 12 follows a clockwise rotating structure from $t^+ = 18.09$ to $t^+ = 25.84$. An attracting LCS encompasses the region exhibiting high swirl strength at the heart of this structure, while secondary LCS, attracting and repelling, enclose pockets of spurts running tangent to the rotation. The clockwise rotation is coupled with a slight downward (negative $z$) motion of $\sim 10\delta_\nu$ over the time depicted. Another interesting structure captured by the LCS in this figure is the $120\delta_\nu$ long streamwise spurt at the bottom of the frames. The interaction of the two structures results in small spots of counterclockwise swirl that can be seen at their interface.

In figure 13, a relatively strong counterclockwise swirl and two weaker clockwise swirls are captured at an early pair of times, figure 13(*a,b*), and a later pair of times, figure 13(*c,d*). These swirls are embedded in a clover-like network of LCS that evolves over the time captured. The primary backbone of this network is formed by an attracting and a repelling LCS that intersect each other. In figure 13(*a*), this intersection is approximately at $(-245, -115)$. Over the time interval shown, the attracting LCS stretches vertically in the vicinity of this intersection. The

https://doi.org/10.1017/jfm.2013.214 Published online by Cambridge University Press

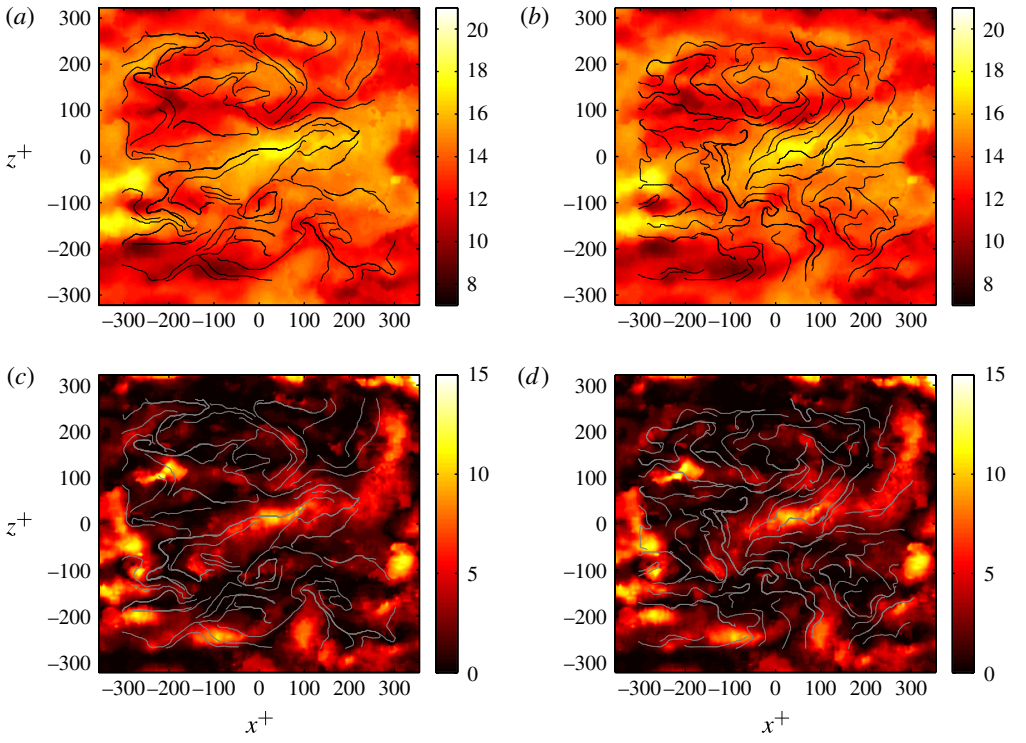



FIGURE 11. (Colour online) Lagrangian coherent structures compared with streamwise velocity and instantaneous turbulent kinetic energy at $t^+ = 11.6$: (*a*) attracting LCS over $U/u_\tau$; (*b*) repelling LCS over $U/u_\tau$; (*c*) attracting LCS over $(u^2 + v^2 + w^2/2u_\tau^2)$; (*d*) repelling LCS over $(u^2 + v^2 + w^2/2u_\tau^2)$.

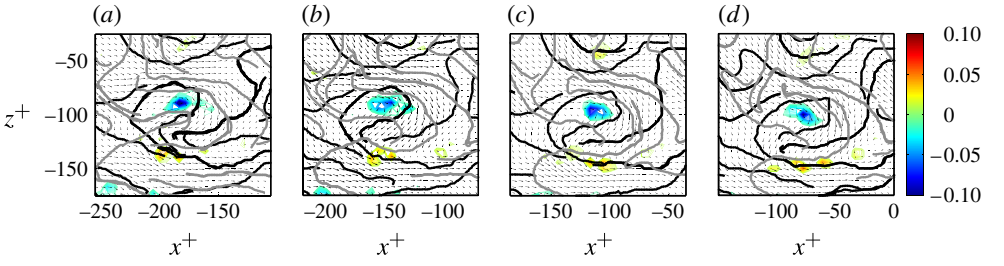



FIGURE 12. (Colour online) Contours of swirl strength highlight a clockwise rotating structure encompassed by LCS over an interval of time: (*a*) $t^+ = 18.09$; (*b*) $t^+ = 20.67$; (*c*) $t^+ = 23.26$; (*d*) $t^+ = 25.84$.

counterclockwise swirl and the clockwise swirl above it appear to be associated with the stretching of this LCS. Also seen here, as noted before with swirls, are spurts that run adjacent to the swirling regions.

In general, the Lagrangian coherent structures are strongly related to structures that can be identified in plots of instantaneous data. This relationship is not surprising since the flow under study demonstrates Taylor's frozen flow hypothesis, and therefore many Eulerian features persist for a significant amount of time. The fact that the LCS

https://doi.org/10.1017/jfm.2013.214 Published online by Cambridge University Press

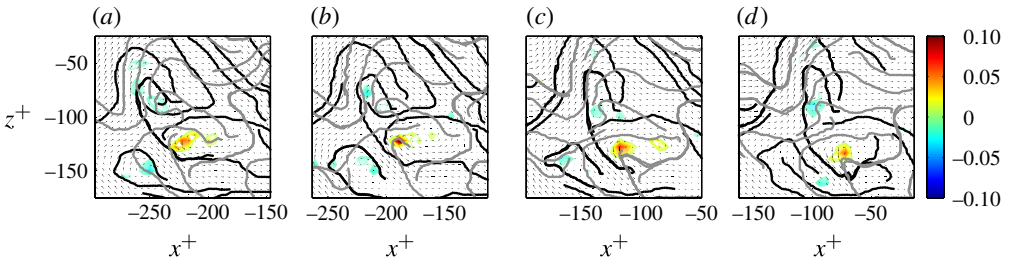



FIGURE 13. (Colour online) Contours of swirl strength highlight counter-rotating structures within a clover-like network of LCS: (*a*) $t^+ = 27.14$; (*b*) $t^+ = 29.72$; (*c*) $t^+ = 34.89$; (*d*) $t^+ = 37.47$.

incorporate several time frames of data does, however, result in some key differences. In particular, even if one frame of velocity data looks like an advection of earlier frames, the computation of LCS considers the movement of fluid, which is by no means frozen. The result is the large-scale association of Eulerian structures that might not be easily recognized from a single frame of instantaneous data.

## 5. Conclusions

In this study, Lagrangian coherent structures are computed on a fixed domain at a sequence of overlapping time intervals using theory and techniques recently developed by Haller (2011) and Farazmand & Haller (2012*a*,*b*). The LCS identified are curves that range in length from $100\delta_\nu$ to $500\delta_\nu$ with various orientations and are distributed throughout the domain. The structures demonstrate a temporal coherence as they appear in consecutive time frames and track with fluid material. Many of the structures can be observed to traverse the entire domain.

Some of the most interesting flow patterns captured occur near the intersections of attracting and repelling LCS. Around such intersections, the fluid tends to display hyperbolic behaviour as theory predicts. When one or both of the LCS involved have some curvature, swirling flow is often observed in one or more of the quadrants formed by the intersection. Figure 14 is a model of an intersection between an attracting and a repelling LCS demonstrating the behaviours observed. The arrows indicate flow direction in an appropriate moving frame.

Collectively, the LCS form an evolving network that separates the flow into distinct regions. The length scales of these regions vary from less than $50\delta_\nu$ up to $300\delta_\nu$. The dynamic behaviour within these regions demonstrates temporal coherence, consistent with the LCS network, as well as spatial coherence, which can be seen, for instance, in the fluctuating velocity field. Many of the individual regions are arranged into clusters forming larger coherent structures with length scales up to $600\delta_\nu$. Often these larger structures identify coherence that would not otherwise be noticed in a single frame of velocity data. The largest scale of organization captured by the LCS is the spanwise arrangement into layers across the domain: tumbleweed-like structures in one type of layer and elongated structures in another. Overall the LCS give a relatively intuitive fingerprint of the turbulence that occurs close to the wall in a turbulent boundary layer. Regions of the fluid that experience a lot of stretching, folding, swirling, etc. are marked with several LCS that are topologically related to these behaviours, while portions of fluid with relatively uniform velocity are marked with very few (if any) LCS.

https://doi.org/10.1017/jfm.2013.214 Published online by Cambridge University Press

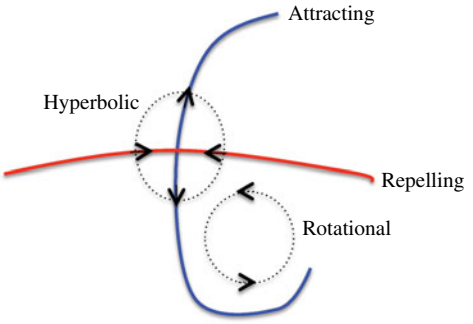



FIGURE 14. (Colour online) Model of flow behaviour often observed near intersections of attracting and repelling LCS.

Even though the applicability and usefulness of planar measurement for the LCS analysis is quantified in this paper, further investigation on the subject is valuable as understanding the entire three-dimensional flow field should elucidate behaviour of the structures not captured by planar analysis, as well as further physics of the problem, thus completing the entire picture. Owing to the low spatial and temporal resolution of three-component volumetric measurements, numerical simulations, in particular DNS or well-resolved large-eddy simulation, can be used. The nature of the problem, however, requires additional computing power in addition to the large demand put on it by the Reynolds number which is quite high in this case. The noise-to-signal ratio increases rapidly as the problem is formulated using three components of the velocity, and it therefore is plausible that this ratio may dominate the problem once the third component in the coordinate system is involved. This remains as an open question.

## Acknowledgements

The authors appreciate the useful discussions and comments by G. Haller, C. Meneveau and J. Riley. This work was funded by the National Science Foundation (CBET-1034581) and the NASA-Oregon Space Grant Consortium. The experiment was conducted under the WALLTURB project, which was funded by the CEC under the 6th framework program (Contract no.: AST4-CT-2005-516008). M. Tutkun acknowledges the partial financial support from The Multiphase Flow Assurance Innovation Centre (FACE).

## REFERENCES

ADRIAN, R. J. 2007 Hairpin vortex organization in wall turbulence. *Phys. Fluids* **19**, 1–54.

ÁLAMO, C. J. & JIMÉNEZ, J. 2009 Estimation of turbulent convection velocities and corrections to Taylor's approximation. *J. Fluid Mech.* **640**, 5–26.

ARNOLD, V. I. 1973 *Ordinary Differential Equations*. MIT Press.

CARLIER, J. & STANISLAS, M. 2005 Experimental study of eddy structures in a turbulent boundary layer using particle image velocimetry. *J. Fluid Mech.* **535**, 143–188.

CHAKRABORTY, P., BALACHANDAR, S. & ADRIAN, R. J. 2005 On the relationships between local vortex identification schemes. *J. Fluid Mech.* **535**, 189–214.

CHONG, M. S., PERRY, A. E. & CANTWELL, B. J. 1990 A general classification of three-dimensional flow fields. *Phys. Fluids* A **2**, 765–777.

https://doi.org/10.1017/jfm.2013.214 Published online by Cambridge University Press

CHONG, P., JINJUN, W. & CAO, Z. 2009 Identification of Lagrangian coherent structures in the turbulent boundary layer. *Sci. China G: Phys. Mech. Astron.* **52**, 248–257.

DENNIS, D. J. C. & NICKELS, T. B. 2008 On the limitations of Taylor's hypothesis in constructing long structures in a turbulent boundary layer. *J. Fluid Mech.* **614**, 197–206.

FARAZMAND, M. & HALLER, G. 2012*a* Computing Lagrangian coherent structures from their variational theory. *Chaos* **22**, 013128–1–12.

FARAZMAND, M. & HALLER, G. 2012*b* Erratum and addendum to 'A variational theory of hyperbolic Lagrangian coherent structures. *Physica* D **240**, 7'. *Physica* D **241**, 439–441.

FOCAUT, J. M., COUDERT, S., KOSTAS, J., STANISLAS, M., BRAUD, P., FOURMENT, C., DELVILLE, J., TUTKUN, M., JOHANSSON, P. & GEORGE, W. K. 2007 Study of the unsteady aspects of turbulence in the near wall region of a boundary layer using High Speed SPIV, In *7th International Symposium on Particle Image Velocimetry*.

GARTH, C., GERHARDT, F., TRICOCHE, X. & HAGEN, H. 2007 Efficient computation and visualization of coherent structures in fluid flow applications. *IEEE Trans. Vis. Comput. Graphics* **13** (6), 1464–1471.

GREEN, M. A., ROWLEY, C. W. & HALLER, G. 2007 Detection of Lagrangian coherent structures in three-dimensional turbulence. *J. Fluid Mech.* **572**, 111–120.

HALLER, G. 2001 Distinguished material surfaces and coherent structures in 3D fluid flows. *Physica* D **149**, 248–277.

HALLER, G. 2005 An objective definition of a vortex. *J. Fluid Mech.* **525**, 1–26.

HALLER, G. 2011 A variational theory of hyperbolic Lagrangian coherent structures. *Physica* D **240**, 574–598.

HINZE, J. O. 1959 *Turbulence*. McGraw Hill.

HUNT, J. C. R., WRAY, A. A. & MOIN, P. 1988 Eddies, stream, and convergence zones in turbulent flows. In *Studying Turbulence Using Numerical Simulation Databases, 2. Proceedings of the 1988 Summer Program* CTR-S88, pp. 193–208. Center for Turbulence Research, Stanford, CA.

JEONG, J. & HUSSEIN, F. 1995 On the identification of a vortex. *J. Fluid Mech.* **285**, 69–94.

LUKENS, S., YANG, X. & FAUCI, L. 2010 Using Lagrangian coherent structures to analyse fluid mixing by cilia. *Chaos* **20**, 017511.

MATHUR, M., HALLER, G., PEACOCK, T., RUPPERT-FELSOT, J. E. & SWINNEY, H. L. 2007 Uncovering the Lagrangian skeleton of turbulence. *Phys. Rev. Lett.* **98**, 144502.

NORGARD, G. & BREMER, P.-T. 2012 Second derivative ridges are straight lines and the implications for computing Lagrangian coherent structures. *Physica* D **241** (18), 1475–1476.

PEIKERT, R., GÜNTHER, D. & WEINKAUF, T. 2013 Comment on 'Second derivative ridges are straight lines and the implications for computing Lagrangian coherent structures, *Physica* D 2012.05.006'. *Physica* D **242** (1), 65–66.

PENG, J. & DABIRI, J. 2008 An overview of a Lagrangian method for analysis of animal wake dynamics. *J. Expl. Biol* **211**, 280–287.

POPE, S. B. 2011 Simple models of turbulent flows. *Phys. Fluids* **23**, 011301.

SHADDEN, S., LEKIEN, F. & MARSDEN, J. 2005 Definition and properties of Lagrangian coherent structures from finite-time Lyapunov exponents in two-dimensional aperiodic flows. *Physica* D **212**, 271–304.

TALLAPRAGADA, P., ROSS, S. D. & SCHMALE, D. G. 2011 Lagrangian coherent structures are associated with fluctuations in airborne microbial populations. *Chaos* **21** (3), 033122.

TANG, W., CHAN, P. W. & HALLER, G. 2010 Accurate extraction of Lagrangian coherent structures over finite domains with application to flight data analysis over Hong Kong International Airport. *Chaos* **20**, 017502.

TANG, W., CHAN, P. W. & HALLER, G. 2011 Lagrangian coherent structure analysis of terminal winds detected by lidar. Part i: turbulence structures. *J. Appl. Meteorol. Climatol.* **50** (2), 325–338.

TAYLOR, G. I. 1938 The spectrum of turbulence. *Proc. R. Soc. Lond.* A **164**, 476–490.

TENNEKES, H. & LUMLEY, J. L. 1972 *A First Course in Turbulence*. The MIT press.

https://doi.org/10.1017/jfm.2013.214 Published online by Cambridge University Press

THEODORSEN, T. 1952 Mechanism of turbulence. In *Proceedings of the 2nd Mid-western Conference on Fluid Mechanics, Ohio State University*, pp. 1–19.

ZHOU, J., ADRIAN, R. J., BALACHANDAR, S. & KENDALL, T. M. 1999 Mechanisms for generating coherent packets of hairpin vortices in channel flow. *J. Fluid Mech.* **387**, 353–396.

https://doi.org/10.1017/jfm.2013.214 Published online by Cambridge University Press